
STRUCTURE-ACCURATE MEDICAL IMAGE TRANSLATION VIA DYNAMIC FREQUENCY BALANCE AND KNOWLEDGE GUIDANCE

Jiahua Xu
Xidian University

Dawei Zhou
Xidian University

Lei Hu
Guangdong Provincial People's Hospital

Zaiyi Liu
Guangdong Provincial People's Hospital

Nannan Wang*
Xidian University

Xinbo Gao
Chongqing University of Posts and Telecommunications

ABSTRACT

Multimodal medical images play a crucial role in the precise and comprehensive clinical diagnosis. Diffusion model is a powerful strategy to synthesize the required medical images. However, existing approaches still suffer from the problem of **anatomical structure distortion** due to the overfitting of high-frequency information and the weakening of low-frequency information. Thus, we propose a novel method based on dynamic frequency balance and knowledge guidance. Specifically, we first extract the low-frequency and high-frequency components by decomposing the critical features of the model using wavelet transform. Then, a **dynamic frequency balance** module is designed to adaptively adjust frequency for enhancing global low-frequency features and effective high-frequency details as well as suppressing high-frequency noise. To further overcome the challenges posed by the large differences between different medical modalities, we construct a **knowledge-guided mechanism** that fuses the prior clinical knowledge from a visual language model with visual features, to facilitate the generation of accurate anatomical structures. Experimental evaluations on multiple datasets show the proposed method achieves significant improvements in qualitative and quantitative assessments, verifying its effectiveness and superiority.

1 Introduction

Multimodal images are crucial for comprehensive evaluation in medical image analysis, which can compensate for the limitations of a single modality and achieve a precise diagnosis [1–3]. In medical image analysis, especially brain tumor diagnosis, computed tomography (CT) and various magnetic resonance (MR) imaging techniques, including T1-weighted, T2-weighted, fluid-attenuated inversion recovery (FLAIR) and diffusion-weighted imaging (DWI), are widely used. Different modalities can provide different contrasts and complementary information for the clinical diagnosis [4–9]. However, in the clinical setting, multimodal image acquisition is often limited by factors such as scanning costs and safety, resulting in missing data for some modalities. The lack of these key modalities can affect the accuracy of clinical diagnosis and treatment. Therefore, how to generate the missing modality using the existing modality has become a key issue in the field of medical research [10–12].

Recently, diffusion models [13, 14] have shown outstanding performance in the field of image-to-image translation [4, 15–17]. It constructs a progressive generation framework by defining the forward process and the reverse process through rigorous mathematical derivation, with a more stable training process and a finer generation quality than GANs (Generative Adversarial Networks) [18]. However, it has been found that existing algorithms based on diffusion

*Corresponding author.

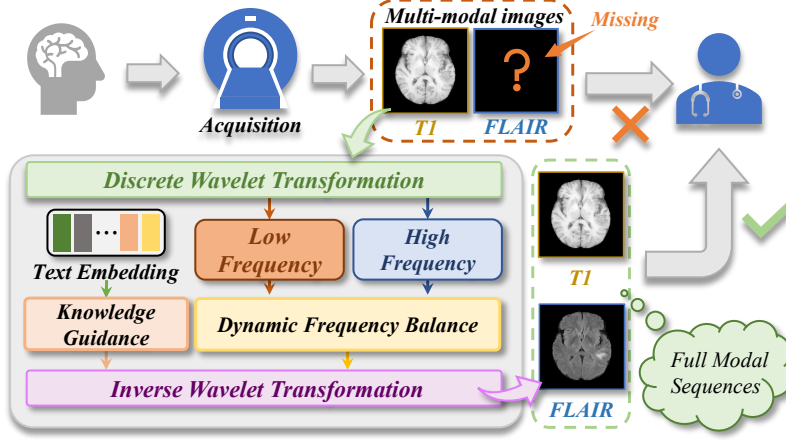


Figure 1: Schematic diagram of our research problem and solution. During medical imaging, certain modalities may be missing due to scanning cost and safety issues. Generating missing modalities via dynamic frequency balance and knowledge guidance can help radiologists make more comprehensive diagnoses.

models have the obvious limitation of overfitting the high-frequency information, which makes it difficult for the model to fully *capture the low-frequency information* of the images. Besides, the generated images are prone to suffer from *anatomical structure distortion* due to the large differences between different medical modalities [19, 20].

To further improve image generation quality, researchers begin to introduce the prior knowledge of vision language model (VLM) into the generation process [21–23]. The pre-trained VLM provides rich prior knowledge for image translation, greatly reducing the learning difficulty while ensuring that the generated images have the correct anatomical structure. However, existing algorithms often *blindly* accept all prior knowledge, resulting in a failure to effectively fuse prior knowledge with the model, which has become a challenge in image translation [24].

To address above issues, as shown in Fig. 1, we propose a structure-accurate translation method called DFBK, which is based on Dynamic Frequency Balance and Knowledge guidance. Specifically, we first extract the low-frequency and high-frequency components by decomposing the critical features of the model using wavelet transform. Subsequently, we designed a dynamic frequency balance module to *adaptively adjust frequency* for enhancing global low-frequency features and effective high-frequency details while suppressing high-frequency noise, thereby facilitating the model to generate correct anatomical structures. To address the challenges posed by the large differences between different medical modalities, we propose a novel knowledge-guided mechanism. The mechanism *fuse prior clinical knowledge with global low-frequency features* using pre-trained VLM. For high-frequency features, we only *retain the critical prior clinical knowledge while suppressing irrelevant information* to avoid the *over-enhancement of high-frequency features*. This mechanism further achieves frequency balance while fusing prior knowledge and avoids the anatomical structure distortion caused by blindly accepting all prior knowledge.

The main contributions are summarized as follows:

- Diffusion model-based medical image translation can trigger anatomical structure distortion due to inappropriate utilization of frequency information, and we propose a novel method DFBK to mitigate this problem.
- We design a dynamic frequency balance module to enhance low-frequency and useful high-frequency components while suppressing high-frequency noise, thus adaptively and optimally leveraging frequency information.
- We construct a knowledge-guided mechanism that fuses prior clinical knowledge with model features, which effectively improves the translation ability against large differences between different medical modalities.
- Our method is evaluated on multiple medical image translation tasks, which exhibits more accurate anatomical structures and superior quantitative metrics scores.

2 Related Work

GAN-based approaches have been widely used in image translation [25–27]. For example, Pix2pix [28] achieves pixel-level synthesis of paired images through a simple network; CycleGAN [29] introduces cyclic consistency loss to

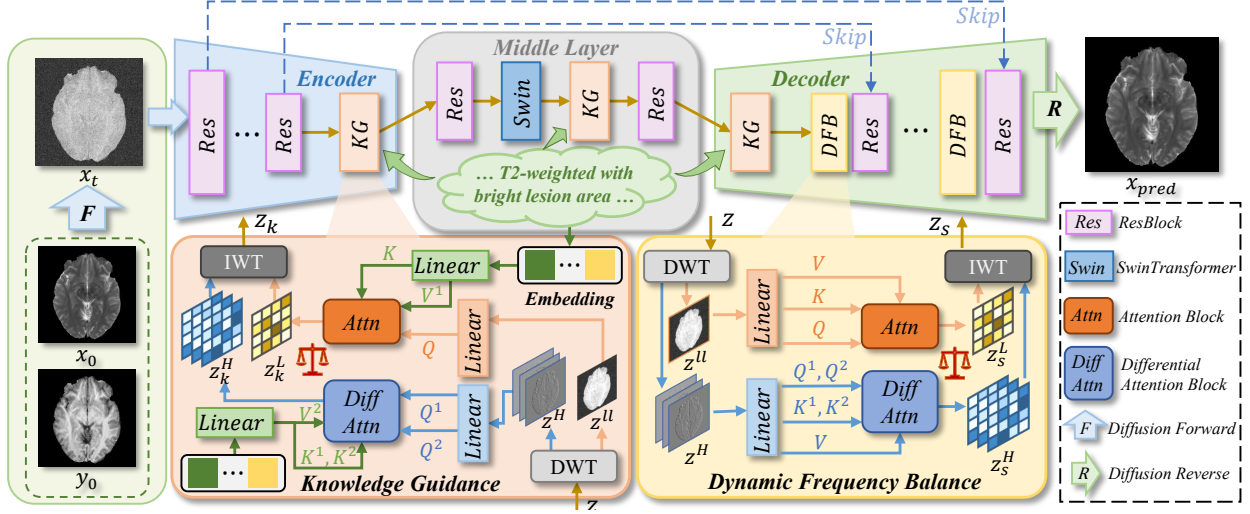


Figure 2: Framework of the proposed method DFBK. In the lower right corner is the Dynamic Frequency Balance module, which achieves frequency balance by adaptively enhancing low-frequency features and effective high-frequency features while suppressing high-frequency noise. In the lower left corner is the Knowledge-Guided mechanism, which fuses the prior knowledge with global low-frequency features and retains only critical prior knowledge and suppresses irrelevant information when fusing with high-frequency features to avoid over-enhancing high-frequency features. Embedding is obtained from the text information using VLM’s text encoder. By using the dynamic frequency balance module and the knowledge-guided mechanism, we can generate target modal images with accurate anatomical structures.

construct cross-domain image mapping. RevGAN [30] is further optimised by designing an approximately reversible architecture to maintain constant memory complexity. Ea-GAN [31] enhances the synthesis of 3D MR images by integrating edge information. ResViT [22] combines a Transformer architecture and fine-tuning techniques to capture contextual features. MaskGAN [32] introduces a mask generator to control the generated region for accurate structure mapping. In order to solve the problem of unstable quality of GAN generated images, SynDiff [17] designed a loop-consistent architecture using a diffusion model to achieve bidirectional inter-modal translation. ResShift [33] designed a diffusion model for direct translation, which reduces the number of diffusion steps and improves the translation efficiency. However, these approaches usually focus excessively on high-frequency features, resulting in inaccurate low-frequency anatomical structures. Therefore, a method is needed to balance the focus on different frequency information.

With the rapid development of VLM, text-driven approaches are gradually applied to image translation [34,35]. Style-CLIP [36] enables CLIP-guided feature manipulation by inverting the source image and obtaining its latent encoding. I2I-Galip [21], on the other hand, uses pre-trained VLM, eliminating the need to individually train the generator-discriminator pairs for each pair of source-target images, thus improving the conversion efficiency and enhancing the accuracy of low-frequency anatomical structures. However, existing algorithms are crude in fusing prior knowledge and are unable to fuse effectively with models. Therefore, there is a need to explore a novel mechanism to effectively fuse prior knowledge to improve model performance.

3 Methodology

3.1 Preliminary

Notice. We use lower-case letters x_0 and y_0 to denote the images of target modality and source modality, respectively. Moreover, we use t to represent the timestep that the diffusion model is going through and T to represent the total number of timesteps. We use the diffusion model based on ResShift and set $t \in \{1, 2, 3, 4\}$. We use $\mathcal{N}(\cdot; \mu, \sigma^2 I)$ to denote a variable that obeys a Gaussian distribution with mean μ and variance matrix σ^2 .

Discrete Wavelet Transformation (DWT). DWT decomposes the image into low-frequency and high-frequency components. The low-frequency component represents the anatomical structure, while the high-frequency components

Algorithm 1 DFBK for medical image translation

Input: $z, c, d, \lambda_q^1, \lambda_q^2, \lambda_k^1, \lambda_k^2, \lambda_{init}$.

Output: The recombination feature z_s and z_k .

```

1:  $z^{ll}, z^{lh}, z^{hl}, z^{hh} \leftarrow DWT(z)$ 
2:  $z^H \leftarrow \text{concat}(z^{lh}, z^{hl}, z^{hh})$ 
3:  $\lambda \leftarrow e^{(\lambda_q^1 \cdot \lambda_k^1)} - e^{(\lambda_q^2 \cdot \lambda_k^2)} + \lambda_{init}$ 
4: if use DFB then
5:    $Q_{z^{ll}}, K_{z^{ll}}, V_{z^{ll}} \leftarrow \text{Linear}(z^{ll})$ 
6:    $z_s^L \leftarrow S(\frac{Q_{z^{ll}} K_{z^{ll}}^T}{\sqrt{d}}) V_{z^{ll}}$ 
7:    $Q_{z^H}, K_{z^H}, V_{z^H} \leftarrow \text{Linear}(z^H)$ 
8:    $z_s^H \leftarrow (S(\frac{Q_{z^H}^1 K_{z^H}^{1T}}{\sqrt{d}}) - \lambda \cdot S(\frac{Q_{z^H}^2 K_{z^H}^{2T}}{\sqrt{d}})) V_{z^H}$ 
9:    $z_s \leftarrow IWT(z_s^L, z_s^H)$  ▷ Dynamic Frequency Balance
10: else if use KG then
11:    $Q_{z^{ll}} \leftarrow \text{Linear}(z^{ll}), K_c, V_c^1 \leftarrow \text{Linear}(c)$ 
12:    $z_k^L \leftarrow S(\frac{Q_{z^{ll}} K_c^T}{\sqrt{d}}) V_c^1$ 
13:    $Q_{z^H}^1, Q_{z^H}^2 \leftarrow \text{Linear}(z^H), K_c^1, K_c^2, V_c^2 \leftarrow \text{Linear}(c)$ 
14:    $z_k^H \leftarrow (S(\frac{Q_{z^H}^1 K_c^{1T}}{\sqrt{d}}) - \lambda \cdot S(\frac{Q_{z^H}^2 K_c^{2T}}{\sqrt{d}})) V_c^2$ 
15:    $z_k \leftarrow IWT(z_k^L, z_k^H)$  ▷ Knowledge Guidance
16: else
17:    $z_s, z_k \leftarrow z$ 
18: end if
19: return  $z_s$  and  $z_k$ 

```

represent the edges and contour details of the image. In this paper, we use Haar wavelet for DWT, which is widely used in applications [37, 38].

Given an image or a feature $z \in \mathbb{R}^{H \times W \times C}$, its low-frequency component $z^{ll} \in \mathbb{R}^{\frac{H}{2} \times \frac{W}{2} \times C}$ and high-frequency components z^{lh}, z^{hl} and $z^{hh} \in \mathbb{R}^{\frac{H}{2} \times \frac{W}{2} \times C}$ can be decomposed by DWT,

$$z^{ll}, z^{lh}, z^{hl}, z^{hh} = DWT(z). \quad (1)$$

DWT can not only effectively decompose frequency components, but also reduce the size of input images or features to reduce computational costs and speed up inference.

ResShift. ResShift uses a custom efficient diffusion process to achieve image translation. Specifically, given a pair of images x_0 and y_0 , the forward process gradually adds noise to x_0 to obtain a Gaussian distribution with y_0 as the mean. This is represented as follows,

$$q(x_t | x_{t-1}, y_0) = \mathcal{N}(x_t; x_{t-1} + \alpha_t e_0, \kappa^2 \alpha_t I), \quad (2)$$

where $e_0 = y_0 - x_0$, which represents the residual between the images of source modality and target modality. $\alpha_t = \eta_t - \eta_{t-1}$, where $\{\eta_t\}_{t=1}^T$ is a sequence that increases monotonically with timestep t and satisfies $\eta_1 \rightarrow 0$ and $\eta_T \rightarrow 1$. κ is a parameter controlling the variance. I is the identity matrix.

Then, we can get the reverse process,

$$q(x_{t-1} | x_t, y_0) = \mathcal{N}\left(x_{t-1}; \mu_\theta(x_t, y_0, t), \kappa^2 \frac{\eta_{t-1}}{\eta_t} \alpha_t I\right), \quad (3)$$

where $\mu_\theta(x_t, y_0, t) = \frac{\eta_{t-1}}{\eta_t} x_t + \frac{\alpha_t}{\eta_t} f_\theta(x_t, y_0, t)$ and f_θ is a neural network with parameter θ used to predict x_0 .

To train the network f_θ , we can obtain the objective function as follows,

$$\min_{\theta} \sum_t \frac{\alpha_t}{2\kappa^2 \eta_t \eta_{t-1}} \|f_\theta(x_t, y_0, t) - x_0\|_2^2. \quad (4)$$

3.2 Medical Image Translation with DFBK

In this section we will introduce the detailed structure of DFBK. The framework is shown in Fig. 2. Firstly, we introduce how to build the dynamic frequency balance module. Then, we will introduce the principles and structure

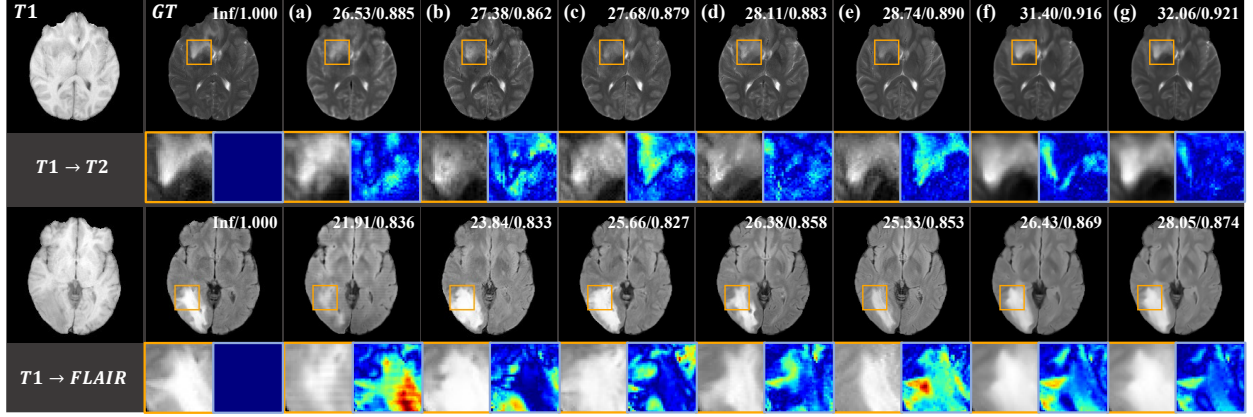


Figure 3: Comparison of approaches on BraTs: (a) Ea-GAN, (b) RevGAN, (c) MaskGAN, (d) ResViT, (e) SynDiff, (f) DFBK (ours). The first and third rows show the results of T1 to T2 and T1 to FLAIR translation, respectively. The first column is the source image, and the second column is the target ground-truth. The second and fourth rows show the zoomed-in anatomical structures for the first and third rows, respectively. PSNR and SSIM values of each image are shown in the corner of images. The yellow box indicates the zoomed-in visualization area, and the blue box represents the difference heatmap between the generated image and the ground truth. The color indicates the degree of difference from small to large, with the brighter color (e.g., red) reflecting the larger difference and vice versa (e.g., blue).

of the knowledge-guided mechanism. Finally, we combine them to obtain a network framework based on dynamic frequency balance and knowledge guidance.

Dynamic Frequency Balance. To address the fact that existing approaches overfit high-frequency information and weaken low-frequency information, resulting in anatomical structure distortion, we proposed a dynamic frequency balance (DFB) module. As shown in Fig. 2, we first use Eq. 1 to decompose the features. Then, we use the self-attention mechanism [39] to enhance the global low-frequency features,

$$z_s^L = S\left(\frac{Q_{z^L} K_{z^L}^T}{\sqrt{d}}\right) V_{z^L}, \quad (5)$$

where $S(\cdot)$ represents the *softmax* function and Q_{z^L} , K_{z^L} , V_{z^L} represent the query, key and value obtained from z^L through a linear layer, respectively. z_s^L is the enhanced low-frequency features and d is the scaling factor.

In order to achieve dynamic frequency balance, we use the differential attention mechanism for high-frequency features,

$$z_s^H = \left(S\left(\frac{Q_{z^H}^1 K_{z^H}^{1T}}{\sqrt{d}}\right) - \lambda \cdot S\left(\frac{Q_{z^H}^2 K_{z^H}^{2T}}{\sqrt{d}}\right) \right) V_{z^H}, \quad (6)$$

where $z^H \in \mathbb{R}^{H \times W \times 3C}$ is obtained by concatenating z^{lh} , z^{hl} and z^{hh} according to channel dimensions. $Q_{z^H}^1$, $Q_{z^H}^2$, $K_{z^H}^1$, $K_{z^H}^2$, and V_{z^H} are all obtained from z^H through a linear layer, where Q and K represent queries and keys, respectively, and V represents the value. λ is a learnable parameter. In order to synchronize the learning dynamics, we re-parameterize λ as follows,

$$\lambda = e^{(\lambda_q^1 \cdot \lambda_k^1)} - e^{(\lambda_q^2 \cdot \lambda_k^2)} + \lambda_{init}, \quad (7)$$

where λ_q^1 , λ_k^2 , λ_q^1 , λ_k^2 are learnable parameters, and λ_{init} is a constant. Differential attention [40] can dynamically filter out and enhance effective high-frequency information while suppressing useless high-frequency noise.

Then, we use the Inverse Wavelet Transformation (IWT) to recombine the frequency features,

$$z_s = IWT(z_s^L, z_s^H), \quad (8)$$

where z_s is the recombination feature. The use of the dynamic frequency balance module can effectively strengthen the model's attention to low-frequency features, while dynamically adjusting the model's attention area for high-frequency features to enhance useful information and suppress high-frequency noise.

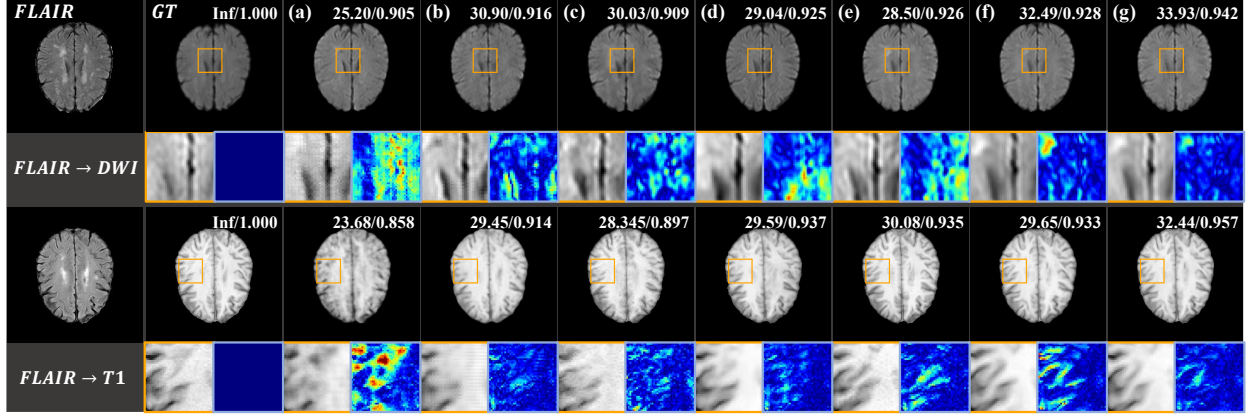


Figure 4: Comparison of approaches on ISLES: (a) Ea-GAN, (b) RevGAN, (c) MaskGAN, (d) ResViT, (e) SynDiff (f) DFBK (ours). The first and third rows show the results of FLAIR to DWI and FLAIR to T1 translation, respectively. The first column is the source image, and the second column is the target ground-truth. The second and fourth rows show the zoomed-in anatomical structures for the first and third rows, respectively.

Knowledge Guidance. In order to effectively introduce VLM’s prior clinical knowledge while ensuring the balance of frequency information, we designed a novel knowledge-guided mechanism (KG) as shown in Fig. 2, which is similar to the dynamic frequency balance module. Specifically, we first fuse prior clinical knowledge and low-frequency features decomposed by Eq. 1,

$$z_k^L = S\left(\frac{Q_{z^L} K_c^T}{\sqrt{d}}\right) V_c^1, \quad (9)$$

where K_c and V_c^1 represent the key and value obtained from the text embedding c through a linear layer, and the text embedding is obtained from the text through the BiomedCLIP’s [41] text encoder.

Then, in order to avoid the over-enhancement of high-frequency features and ensure the frequency balance, we use differential cross attention to fuse high-frequency features with prior clinical knowledge,

$$z_k^H = \left(S\left(\frac{Q_{z^H}^1 K_c^{1T}}{\sqrt{d}}\right) - \lambda \cdot S\left(\frac{Q_{z^H}^2 K_c^{2T}}{\sqrt{d}}\right) \right) V_c^2, \quad (10)$$

where K_c^1 , K_c^2 and V_c^2 are all obtained from the text embedding through a linear layer.

Finally, we can obtain the recombination feature z_k ,

$$z_k = IWT(z_k^L, z_k^H). \quad (11)$$

Through the dynamic frequency balance module and the knowledge guidance mechanism, we can balance the model’s ability to extract features of high and low frequency information, thereby generating accurate anatomical structures.

Overall Framework. We choose SwinUNet [42] as the base framework. Since the frequency balance in the backbone features is particularly important [19], we use the frequency balance module on backbone features before skipping connection. In addition, introducing prior knowledge in all layers can lead to fusion mismatch, and introducing it in bottom layers is more effective [43], so we decide to use the knowledge-guided mechanism in bottom layers. The details of the overall process are presented in Algorithm 1.

4 Implementation Details

4.1 Experimental Datasets

We utilize three public datasets for the evaluation and validation of DFBK. We use the Brain Tumor Segmentation challenge 2023 (BraTs 2023) [5, 44–46] dataset to perform common translation tasks such as T1 to T2 and T1 to FLAIR. In addition, we also perform experiments on rare translation tasks such as FLAIR to DWI and FLAIR to T1

Table 1: Quantitative comparison of different approaches on BraTs and ISLSE. The values in the table represent the average values for the entire test dataset, and higher values are better. **Bold** indicates the best result, and underlined indicates the suboptimal result.

Dataset	BraTs (2023)				ISLES (2015)			
	T1→T2		T1→FLAIR		FLAIR→DWI		FLAIR→T1	
Method	PSNR ↑	SSIM ↑	PSNR ↑	SSIM ↑	PSNR ↑	SSIM ↑	PSNR ↑	SSIM ↑
Ea-GAN	22.43	<u>0.825</u>	21.16	0.773	24.18	0.850	21.35	0.810
RevGAN	22.61	0.816	21.83	0.769	25.40	0.862	23.64	0.844
MaskGAN	21.40	0.809	20.41	0.735	25.24	0.856	23.15	0.834
ResViT	<u>22.89</u>	0.822	<u>21.87</u>	<u>0.786</u>	<u>25.67</u>	0.872	<u>24.90</u>	<u>0.873</u>
SynDiff	21.68	0.814	20.41	0.755	25.39	<u>0.872</u>	24.32	0.867
DFBK (ours)	23.61	0.846	22.38	0.797	25.76	0.879	25.42	0.879

using Ischemic Stroke Lesion Segmentation challenge 2015 (ISLES 2015) [47, 48]. To further verify the generalization ability, we also perform experiments on complex translation tasks of CT and MR using Synthesizing computed tomography for Radiotherapy 2023 (SynthRAD 2023) [49].

For BraTs dataset, we select 40,032 images from 1,251 subjects with 32 images per subject for training. Additionally, 7,008 images were chosen from 219 subjects with 32 images per subject for generating the target modality and evaluation. For ISLES dataset, we select 1,792 images from 28 subjects with 64 images per subject for training and 2,304 images from 36 subjects with 64 images per subject for evaluation. For SynthRAD dataset, we select 9,216 images from 144 subjects with 64 images per subject for training and 2,304 images from 36 subjects with 64 images per subject for evaluation. The more information is available in Supplementary Material A.

4.2 Comparison Approaches

We select three classes of approaches for comparison. The first is GANs-based approaches, EaGAN, RevGAN and MaskGAN. The second is transformer-based approach, ResViT, which is a large model fine-tuning approach. The third is SynDiff which is based on diffusion model. The training parameters are set according to the parameters specified in the original paper, respectively. We use two evaluation metrics, peak signal-to-noise ratio (PSNR) and structural similarity index measure (SSIM) to quantitatively evaluate the generated results to verify the effectiveness of our method.

5 Experimental Results

5.1 Qualitative Results

Fig. 3 shows the results of various methods for medical image translation on BraTs. Ea-GAN introduces grating-like artifacts, and the anatomical structure in some areas is very blurred or even completely distorted as shown in Fig. 3 (a). RevGAN has unrecognizable anatomical structures and introduces additional lesion areas (Fig. 3 (b)). MaskGAN suffers from generating incorrect content and the synthesized images appearing overly blurred (Fig. 3 (c)). ResViT generates a relatively correct anatomical structure, but the brightness of some areas does not match the target modality (Fig. 3 (d)). The anatomical structure generated by SynDiff is incorrect, and the brightness do not match the target modality (Fig. 3 (e)). In contrast, the images generated by our proposed method demonstrate significantly improved anatomical accuracy and more precise contrast representation. As shown in Figure 3 (f), our approach effectively preserves the structural integrity of anatomical features while maintaining the correct brightness distribution according to target modality. Furthermore, our method achieves the better performance across the quantitative evaluation metrics, underscoring its superiority in medical image translation.

Fig. 4 shows the results of various methods for medical image translation on ISLES. Ea-GAN cannot generate the correct anatomical structure, and the content is completely distorted, as shown in Figure 4 (a). RevGAN introduces faint raster-like artifacts, and some areas are distorted (Figure 4 (b)). MaskGAN generates blurry content (Figure 4 (c)). The anatomical structure generated by ResViT (Figure 4 (d)) and SynDiff (Figure 4 (e)) exhibits noticeable incorrect, with significant distortions in shape and structure. In contrast, as shown in Figure 4 (f), our method presents more accurate anatomical structures and achieves better metric values.

We also shows the results on the difficult task of CT to MR translation on SynthRAD, as shown in Fig. 5 in Supplementary Material B. Since CT images do not provide information about the internal anatomical structure of the brain,

Table 2: Quantitative comparison of different approaches on SynthRAD.

Dataset	SynthRAD (2023)			
	MR->CT		CT->MR	
Method	PSNR \uparrow	SSIM \uparrow	PSNR \uparrow	SSIM \uparrow
Ea-GAN	24.75	0.852	20.39	0.679
RevGAN	26.24	0.872	22.94	0.798
MaskGAN	25.56	0.871	22.04	0.761
ResViT	<u>26.92</u>	<u>0.887</u>	22.88	<u>0.801</u>
SynDiff	26.05	0.877	20.73	0.705
DFBK (ours)	27.51	0.897	23.54	0.828

Table 3: Ablation study on Dynamic Frequency Balance (DFB) and Knowledge Guidance (KG). “None” indicates the performances in the absence of DFB and KG.

Task	FLAIR->DWI		FLAIR->T1	
Method	PSNR \uparrow	SSIM \uparrow	PSNR \uparrow	SSIM \uparrow
None	25.61	0.877	25.15	0.876
+DFB	25.70	0.878	25.21	0.877
+KG	25.68	0.877	25.31	0.878
+DFB, KG	25.76	0.879	25.42	0.879

most approaches cannot generate correct or relevant target modality anatomical structures. As shown in Fig. 5 (a), Ea-GAN produces MR images with raster artifacts and lacks clear internal anatomical structures, while its CT images show blurred cranial boundaries. RevGAN can generate relevant MR structures but fails to delineate the lesion area, and its CT images also have blurred cranial boundaries (Fig. 5 (b)). MaskGAN confuses the lesion with normal brain structures in the MR images, and its CT images exhibit incorrect cranial boundaries (Fig. 5 (c)). Although ResViT (Fig. 5 (d)) and SynDiff (Fig. 5 (e)) localize the lesion area in generated MR images, they do not accurately reproduce the overall internal anatomy and CT images generated by ResViT miss part of the cranial boundaries. In contrast, our method accurately localizes the MR lesion area, generates correct anatomical structures, and produces CT images with correct cranial boundaries (Fig. 5 (f)). The more visualization results are in Supplementary Material B.

5.2 Quantitative Results

Tab. 1 and Tab. 2 shows the mean values for each quantitative metric, where higher PSNR and SSIM values perform better. Our method outperforms all other approaches in six translation tasks on three datasets. Its superior performance stems from effectively balancing the model’s extraction of high- and low-frequency information and effective prior knowledge guidance, thereby preventing anatomical distortions caused by too fast high-frequency convergence and insufficient low-frequency extraction. In contrast, GAN-based approaches produce poor results due to their inherent instability in training, which makes them particularly susceptible to outliers in low-quality datasets such as BraTs. SynDiff, which incorporates GAN principles into a diffusion model, also shows unsatisfactory performance because its more complex training process is more sensitive to data quality. ResViT achieves relatively good results by leveraging large model fine-tuning, but still causes anatomical distortion. In contrast, our method effectively achieves frequency balance and has better performance.

5.3 Ablation Study

In this section, we validate the effectiveness of dynamic frequency balance module and knowledge-guided mechanism. All experiments are performed on ISLES dataset.

Dynamic Frequency Balance module (DFB) and Knowledge-Guided mechanism (KG). We conduct ablation experiments on the dynamic frequency balance module and the knowledge-guided mechanism to verify their important roles in medical image translation.

From Tab. 3, we can see that both dynamic frequency balance and knowledge guidance play an important role in generating the correct anatomical structure and affect most indicators, such as PSNR and SSIM. At the same time, it can be seen that when the source modality and target modality are significantly different, such as the conversion from FLAIR to T1, the knowledge-guided mechanism plays an important role and can effectively guide the model to generate correct anatomical structures.

The components in DFB. It can be seen from Tab. 4 that only enhancing the low-frequency features (L) can alleviate the poor performance of the model due to too fast high-frequency convergence to a certain extent, while only dynamically balancing the high-frequency features (H) suppresses some high-frequency noise, but the enhancement of the effective high-frequency components actually accelerates the high-frequency convergence of the model and reduces the performance. The improvement of PSNR in the FLAIR to DWI task is related to its similar modality. To further demonstrate the importance of frequency balance, we replace the dynamic frequency balance module with a normal self-attention mechanism (NormAttn). The results show that the performance of the model has slightly decreased. This is because the self-attention mechanism can only enhance global features, but cannot balance high-frequency

Table 4: Ablation study on the components in the Dynamic Frequency Balance module. “None” indicates the performances when there are no additional operations in this module.

Task	FLAIR→DWI		FLAIR→T1	
Method	PSNR ↑	SSIM ↑	PSNR ↑	SSIM ↑
None	25.61	0.877	25.15	0.876
+L	25.65	0.878	25.17	0.876
+H	25.67	0.877	25.12	0.874
+NormAttn	25.59	0.878	25.09	0.874
+L, H	25.70	0.878	25.21	0.877

Table 5: Ablation study on the components in the Knowledge-Guided mechanism. “None” indicates the performances when there are no additional operations in this mechanism.

Task	FLAIR→DWI		FLAIR→T1	
Method	PSNR ↑	SSIM ↑	PSNR ↑	SSIM ↑
None	25.61	0.877	25.15	0.876
+L	25.66	0.876	25.21	0.878
+H	25.59	0.875	25.15	0.874
+CrossAttn	25.64	0.877	25.21	0.875
+L, H	25.68	0.877	25.31	0.878

and low-frequency features, which makes the model further strengthen the convergence of high-frequency features. In contrast, the dynamic frequency balance module can decompose and process frequency components more carefully.

The components in KG. As shown in Tab. 5, only fusing the prior knowledge with low-frequency features can guide the model to enhance the extraction of low-frequency features and slightly improve the model performance. However, only fusing the prior knowledge with high-frequency features cannot achieve frequency balance, even if the enhancement of high-frequency features is suppressed. This shows that the enhancement of low-frequency is more important. To further verify the effectiveness of the knowledge-guided mechanism, we replaced it with a cross-attention mechanism (CrossAttn). The results show that the cross-attention mechanism can slightly improve the model performance, but it limits the guidance of the model by the prior knowledge due to the over-enhancement of high-frequency. In contrast, the knowledge-guided mechanism processes high and low frequencies separately, effectively improving model performance.

6 Conclusion

In this paper, we propose a new diffusion model architecture for medical image translation, which achieves generating target modalities with correct anatomical structures through the dynamic frequency balance module and the knowledge-guided mechanism. Experimental results demonstrate our method’s effectiveness in medical image translation and excellent performance in generating correct anatomical structures. Ablation experiments also demonstrate the effectiveness of our proposed dynamic frequency balance module and knowledge-guided mechanism.

Limitation. A major limitation of this study is that our method relies on high-quality paired data, but it may be difficult to obtain a large number of paired images due to the variety of factors, which may influence its broad applicability in some clinical scenarios. To overcome this limitation, our future research will focus on exploring medical image translation based on unpaired images.

In summary, we propose a novel method for structure-accurate medical image translation, which aims to overcome the interference of modality absence on clinical diagnosis. The proposed method is expected to facilitate radiologists in making more precise diagnoses.

References

- [1] Cirong Liu, Q Ye Frank, Cecil Chern-Chyi Yen, John D Newman, Daniel Glen, David A Leopold, and Afonso C Silva. A digital 3d atlas of the marmoset brain based on multi-modal mri. *Neuroimage*, 169:106–116, 2018.
- [2] Yan Shen and Mingchen Gao. Brain tumor segmentation on mri with missing modalities. In *Information Processing in Medical Imaging: 26th International Conference, IPMI 2019, Hong Kong, China, June 2–7, 2019, Proceedings 26*, pages 417–428. Springer, 2019.
- [3] Tong Tong, Katherine Gray, Qinquan Gao, Liang Chen, Daniel Rueckert, Alzheimer’s Disease Neuroimaging Initiative, et al. Multi-modal classification of alzheimer’s disease using nonlinear graph fusion. *Pattern recognition*, 63:171–181, 2017.
- [4] Jonghun Kim and Hyunjin Park. Adaptive latent diffusion model for 3d medical image to image translation: Multi-modal magnetic resonance imaging study. In *Proceedings of the IEEE/CVF Winter Conference on Applications of Computer Vision*, pages 7604–7613, 2024.

- [5] Bjoern H Menze, Andras Jakab, Stefan Bauer, Jayashree Kalpathy-Cramer, Keyvan Farahani, Justin Kirby, Yuliya Burren, Nicole Porz, Johannes Slotboom, Roland Wiest, et al. The multimodal brain tumor image segmentation benchmark (brats). *IEEE transactions on medical imaging*, 34(10):1993–2024, 2014.
- [6] Gaurav Shukla, Gregory S Alexander, Spyridon Bakas, Rahul Nikam, Kiran Talekar, Joshua D Palmer, and Wenying Shi. Advanced magnetic resonance imaging in glioblastoma: a review. *Chinese clinical oncology*, 6(4):40–40, 2017.
- [7] Sohil H Patel, Laila M Poisson, Daniel J Brat, Yueren Zhou, Lee Cooper, Matija Snuderl, Cheddhi Thomas, Ana M Franceschi, Brent Griffith, Adam E Flanders, et al. T2–flair mismatch, an imaging biomarker for idh and 1p/19q status in lower-grade gliomas: a tcga/tcia project. *Clinical cancer research*, 23(20):6078–6085, 2017.
- [8] J Mintonovitch, ME Moseley, L Chileuitt, H Shimizu, Y Cohen, and PR Weinstein. Comparison of diffusion- and t2-weighted mri for the early detection of cerebral ischemia and reperfusion in rats. *Magnetic resonance in medicine*, 18(1):39–50, 1991.
- [9] Michael E Moseley, Y Cohen, J Mintonovitch, L Chileuitt, H Shimizu, J Kucharczyk, MF Wendland, and PR Weinstein. Early detection of regional cerebral ischemia in cats: comparison of diffusion- and t2-weighted mri and spectroscopy. *Magnetic resonance in medicine*, 14(2):330–346, 1990.
- [10] Dinggang Shen, Guorong Wu, and Heung-II Suk. Deep learning in medical image analysis. *Annual review of biomedical engineering*, 19(1):221–248, 2017.
- [11] Stef Van Buuren, Hendrick C Boshuizen, and Dick L Knook. Multiple imputation of missing blood pressure covariates in survival analysis. *Statistics in medicine*, 18(6):681–694, 1999.
- [12] Willi Sauerbrei and Patrick Royston. Building multivariable prognostic and diagnostic models: transformation of the predictors by using fractional polynomials. *Journal of the Royal Statistical Society: Series A (Statistics in Society)*, 162(1):71–94, 1999.
- [13] Jiaming Song, Chenlin Meng, and Stefano Ermon. Denoising diffusion implicit models. *arXiv preprint arXiv:2010.02502*, 2020.
- [14] Jonathan Ho, Ajay Jain, and Pieter Abbeel. Denoising diffusion probabilistic models. *Advances in neural information processing systems*, 33:6840–6851, 2020.
- [15] Kyobin Choo, Youngjun Jun, Mijin Yun, and Seong Jae Hwang. Slice-consistent 3d volumetric brain ct-to-mri translation with 2d brownian bridge diffusion model. In *International Conference on Medical Image Computing and Computer-Assisted Intervention*, pages 657–667. Springer, 2024.
- [16] Dac Thai Nguyen, Trung Thanh Nguyen, Huu Tien Nguyen, Thanh Trung Nguyen, Huy Hieu Pham, Thanh Hung Nguyen, Thao Nguyen Truong, and Phi Le Nguyen. Ct to pet translation: A large-scale dataset and domain-knowledge-guided diffusion approach. *arXiv preprint arXiv:2410.21932*, 2024.
- [17] Muzaffer Özbey, Onat Dalmaz, Salman UH Dar, Hasan A Bedel, Şaban Öztürk, Alper Güngör, and Tolga Çukur. Unsupervised medical image translation with adversarial diffusion models. *IEEE Transactions on Medical Imaging*, 2023.
- [18] Prafulla Dhariwal and Alexander Nichol. Diffusion models beat gans on image synthesis. *Advances in neural information processing systems*, 34:8780–8794, 2021.
- [19] Chenyang Si, Ziqi Huang, Yuming Jiang, and Ziwei Liu. Freeu: Free lunch in diffusion u-net. In *Proceedings of the IEEE/CVF Conference on Computer Vision and Pattern Recognition*, pages 4733–4743, 2024.
- [20] Xiongye Xiao, Shixuan Li, Luzhe Huang, Gengshuo Liu, Trung-Kien Nguyen, Yi Huang, Di Chang, Mykel J Kochenderfer, and Paul Bogdan. Multi-scale generative modeling for fast sampling. *arXiv preprint arXiv:2411.09356*, 2024.
- [21] Yilmaz Korkmaz and Vishal M Patel. I2i-galip: Unsupervised medical image translation using generative adversarial clip. *arXiv preprint arXiv:2409.12399*, 2024.
- [22] Onat Dalmaz, Mahmut Yurt, and Tolga Çukur. Resvit: residual vision transformers for multimodal medical image synthesis. *IEEE Transactions on Medical Imaging*, 41(10):2598–2614, 2022.
- [23] Dongxu Li, Junnan Li, and Steven Hoi. Blip-diffusion: Pre-trained subject representation for controllable text-to-image generation and editing. *Advances in Neural Information Processing Systems*, 36, 2024.
- [24] Enze Xie, Junsong Chen, Junyu Chen, Han Cai, Haotian Tang, Yujun Lin, Zhekai Zhang, Muyang Li, Ligeng Zhu, Yao Lu, et al. Sana: Efficient high-resolution image synthesis with linear diffusion transformers. *arXiv preprint arXiv:2410.10629*, 2024.

- [25] Karim Armanious, Chenming Jiang, Sherif Abdulatif, Thomas Küstner, Sergios Gatidis, and Bin Yang. Unsupervised medical image translation using cycle-medgan. In *2019 27th European signal processing conference (EUSIPCO)*, pages 1–5. IEEE, 2019.
- [26] Karim Armanious, Aastha Tanwar, Sherif Abdulatif, Thomas Küstner, Sergios Gatidis, and Bin Yang. Unsupervised adversarial correction of rigid mr motion artifacts. In *2020 IEEE 17th International Symposium on Biomedical Imaging (ISBI)*, pages 1494–1498. IEEE, 2020.
- [27] Hyungjin Chung, Jaehyun Kim, Jeong Hee Yoon, Jeong Min Lee, and Jong Chul Ye. Simultaneous super-resolution and motion artifact removal in diffusion-weighted mri using unsupervised deep learning. *arXiv preprint arXiv:2105.00240*, 2021.
- [28] Phillip Isola, Jun-Yan Zhu, Tinghui Zhou, and Alexei A Efros. Image-to-image translation with conditional adversarial networks. In *Proceedings of the IEEE conference on computer vision and pattern recognition*, pages 1125–1134, 2017.
- [29] Jun-Yan Zhu, Taesung Park, Phillip Isola, and Alexei A Efros. Unpaired image-to-image translation using cycle-consistent adversarial networks. In *Proceedings of the IEEE international conference on computer vision*, pages 2223–2232, 2017.
- [30] Tycho FA van der Ouderaa and Daniel E Worrall. Reversible gans for memory-efficient image-to-image translation. In *Proceedings of the IEEE/CVF Conference on Computer Vision and Pattern Recognition*, pages 4720–4728, 2019.
- [31] Biting Yu, Luping Zhou, Lei Wang, Yinghuan Shi, Jurgen Fripp, and Pierrick Bourgeat. Ea-gans: edge-aware generative adversarial networks for cross-modality mr image synthesis. *IEEE transactions on medical imaging*, 38(7):1750–1762, 2019.
- [32] Vu Minh Hieu Phan, Zhibin Liao, Johan W Verjans, and Minh-Son To. Structure-preserving synthesis: Maskgan for unpaired mr-ct translation. In *International Conference on Medical Image Computing and Computer-Assisted Intervention*, pages 56–65. Springer, 2023.
- [33] Zongsheng Yue, Jianyi Wang, and Chen Change Loy. Efficient diffusion model for image restoration by residual shifting. *IEEE Transactions on Pattern Analysis and Machine Intelligence*, 2024.
- [34] Kaede Shiohara and Toshihiko Yamasaki. Face2diffusion for fast and editable face personalization. In *Proceedings of the IEEE/CVF Conference on Computer Vision and Pattern Recognition*, pages 6850–6859, 2024.
- [35] Hao Fei, Shengqiong Wu, Wei Ji, Hanwang Zhang, and Tat-Seng Chua. Dysen-vdm: Empowering dynamics-aware text-to-video diffusion with llms. In *Proceedings of the IEEE/CVF Conference on Computer Vision and Pattern Recognition*, pages 7641–7653, 2024.
- [36] Or Patashnik, Zongze Wu, Eli Shechtman, Daniel Cohen-Or, and Dani Lischinski. Styleclip: Text-driven manipulation of stylegan imagery. In *Proceedings of the IEEE/CVF international conference on computer vision*, pages 2085–2094, 2021.
- [37] Hao Phung, Quan Dao, and Anh Tran. Wavelet diffusion models are fast and scalable image generators. In *Proceedings of the IEEE/CVF conference on computer vision and pattern recognition*, pages 10199–10208, 2023.
- [38] Yunqi Miao, Jiankang Deng, and Jungong Han. Waveface: Authentic face restoration with efficient frequency recovery. In *Proceedings of the IEEE/CVF Conference on Computer Vision and Pattern Recognition*, pages 6583–6592, 2024.
- [39] Ashish Vaswani, Noam Shazeer, Niki Parmar, Jakob Uszkoreit, Llion Jones, Aidan N Gomez, Łukasz Kaiser, and Illia Polosukhin. Attention is all you need. *Advances in neural information processing systems*, 30, 2017.
- [40] Tianzhu Ye, Li Dong, Yuqing Xia, Yutao Sun, Yi Zhu, Gao Huang, and Furu Wei. Differential transformer. *arXiv preprint arXiv:2410.05258*, 2024.
- [41] Sheng Zhang, Yanbo Xu, Naoto Usuyama, Jaspreet Bagga, Robert Tinn, Sam Preston, Rajesh Rao, Mu Wei, Naveen Valluri, Cliff Wong, et al. Large-scale domain-specific pretraining for biomedical vision-language processing. *arXiv preprint arXiv:2303.00915*, 2(3):6, 2023.
- [42] Ze Liu, Yutong Lin, Yue Cao, Han Hu, Yixuan Wei, Zheng Zhang, Stephen Lin, and Baining Guo. Swin transformer: Hierarchical vision transformer using shifted windows. In *Proceedings of the IEEE/CVF international conference on computer vision*, pages 10012–10022, 2021.
- [43] Haofan Wang, Matteo Spinelli, Qixun Wang, Xu Bai, Zekui Qin, and Anthony Chen. Instantstyle: Free lunch towards style-preserving in text-to-image generation. *arXiv preprint arXiv:2404.02733*, 2024.

- [44] Spyridon Bakas, Hamed Akbari, Aristeidis Sotiras, Michel Bilello, Martin Rozycki, JS Kirby, JB Freymann, Keyvan Farahani, and Christos Davatzikos. Segmentation labels and radiomic features for the pre-operative scans of the tcga-lgg collection [data set]. the cancer imaging archive, 2017.
- [45] Spyridon Bakas, Hamed Akbari, Aristeidis Sotiras, Michel Bilello, Martin Rozycki, Justin S Kirby, John B Freymann, Keyvan Farahani, and Christos Davatzikos. Advancing the cancer genome atlas glioma mri collections with expert segmentation labels and radiomic features. *Scientific data*, 4(1):1–13, 2017.
- [46] Ujjwal Baid, Satyam Ghodasara, Suyash Mohan, Michel Bilello, Evan Calabrese, Errol Colak, Keyvan Farahani, Jayashree Kalpathy-Cramer, Felipe C Kitamura, Sarthak Pati, et al. The rsna-asnr-miccai brats 2021 benchmark on brain tumor segmentation and radiogenomic classification. *arXiv preprint arXiv:2107.02314*, 2021.
- [47] Oskar Maier, Bjoern H Menze, Janina Von der Gablentz, Levin Häni, Mattias P Heinrich, Matthias Liebrand, Stefan Winzeck, Abdul Basit, Paul Bentley, Liang Chen, et al. Isles 2015-a public evaluation benchmark for ischemic stroke lesion segmentation from multispectral mri. *Medical image analysis*, 35:250–269, 2017.
- [48] Oskar Maier, Matthias Wilms, Janina von der Gablentz, Ulrike M Krämer, Thomas F Münte, and Heinz Handels. Extra tree forests for sub-acute ischemic stroke lesion segmentation in mr sequences. *Journal of neuroscience methods*, 240:89–100, 2015.
- [49] Adrian Thummerer, Erik van der Bijl, Arthur Galapon Jr, Joost JC Verhoeff, Johannes A Langendijk, Stefan Both, Cornelis (Nico) AT van den Berg, and Matteo Maspero. Synthrad2023 grand challenge dataset: Generating synthetic ct for radiotherapy. *Medical physics*, 50(7):4664–4674, 2023.

Supplementary Material

A Experimental Details

A.1 Datasets

Brain Tumor Segmentation challenge 2023 (BraTs 2023). BraTs dataset has 1251 subjects for training and 219 subjects for evaluation, each subject has 155 slices and each slice size is 240×240 . We select 40,032 images from 1,251 subjects with 32 images per subject in the training set for model training. Additionally, 7008 images were chosen from 219 subjects in the validation set, with 32 images per subject for generating the target modality and evaluation. All images are center-cropped and resize to the size of 192×192 to remove redundant areas that do not contain brain information.

Ischemic Stroke Lesion Segmentation challenge 2015 (ISLES 2015). ISLES dataset has 28 subjects for training and 36 subjects for evaluation. The number and size of slices in each subject are inconsistent. We select 1,792 images from 28 subjects with 64 images per subject in the training set for model training. Additionally, 2,304 images were chosen from 36 subjects in the validation set, with 64 images per subject for generating the target modality and evaluation. All images are center-cropped and resize to the size of 224×224 to remove redundant areas that do not contain brain information.

Synthesizing computed tomography for Radiotherapy 2023 (SynthRAD 2023). ISLES dataset has 144 subjects for training and 36 subjects for evaluation. The number and size of slices in each subject are inconsistent. We select 9,216 images from 144 subjects with 64 images per subject in the training set for model training, and 2,304 images were chosen from 36 subjects in the validation set, with 64 images per subject for generating the target modality and evaluation. All images are center-cropped and resize to the size of 192×192 to remove redundant areas that do not contain brain information.

A.2 Training Details

Our method’s training is based on ResShift and SwinUNet. We set the number of the channel dimensions to 160, the number of head channels to 32, the number of residual block to 2, the swin depth to 2, and the swin embedding dim to 256. The channel multipliers are set to $\{1, 1, 2, 2, 4\}$ and $\{1, 1, 2, 2, 4, 4\}$ for size 224 and 192, respectively. We set the batch size to 1 for ISLES dataset and 4 for BraTs and SynthRAD datasets, the total number of timesteps to 4, the window size to 14 for ISLES dataset and 8 for BraTs and SynthRAD datasets, and learning rate to 5.0×10^{-5} which is reduced by cosine to 2.0×10^{-5} . We trained the model with 100k iterations. The diffusion model training is conducted on two RTX 4090 GPUs.

B Additional Experimental Results

As shown in Fig. 5, 6, 7 and 8, our method consistently outperforms other methods for medical image translation on BraTs, ISLES, and SynthRAD datasets, demonstrating superior anatomical accuracy, and better quantitative metrics. Unlike other methods, our approach effectively maintains structural integrity, accurately locates lesion areas, and ensures realistic conversion between imaging modalities. Therefore, our method is robust and reliable in medical image translation and has great clinical application value.

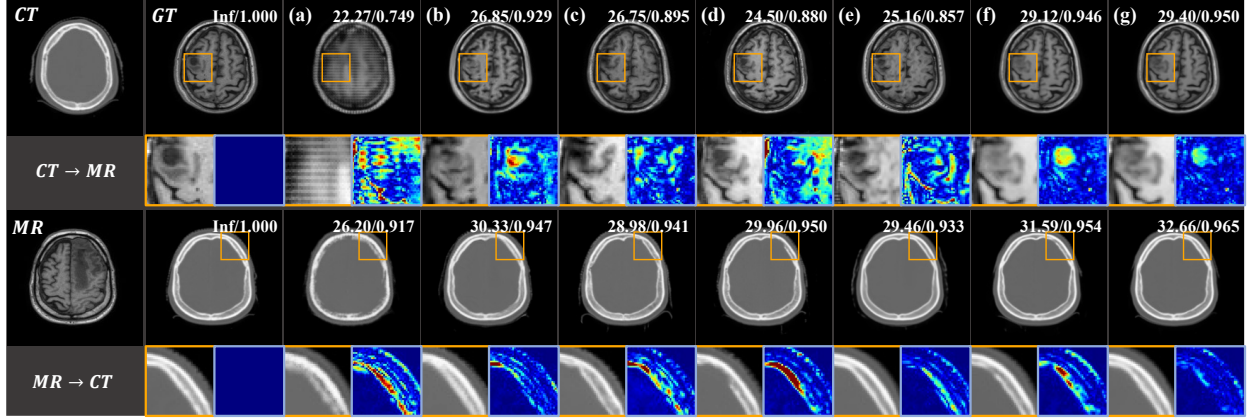


Figure 5: Comparison of approaches on SynthRAD: (a) Ea-GAN, (b) RevGAN, (c) MaskGAN, (d) ResViT, (e) SynDiff (f) DFBK (ours). The first and third rows show the results of CT to MR and MR to CT translation, respectively. The first column is the source image, and the second column is the target ground-truth. The second and fourth rows show the zoomed-in anatomical structures for the first and third rows, respectively.

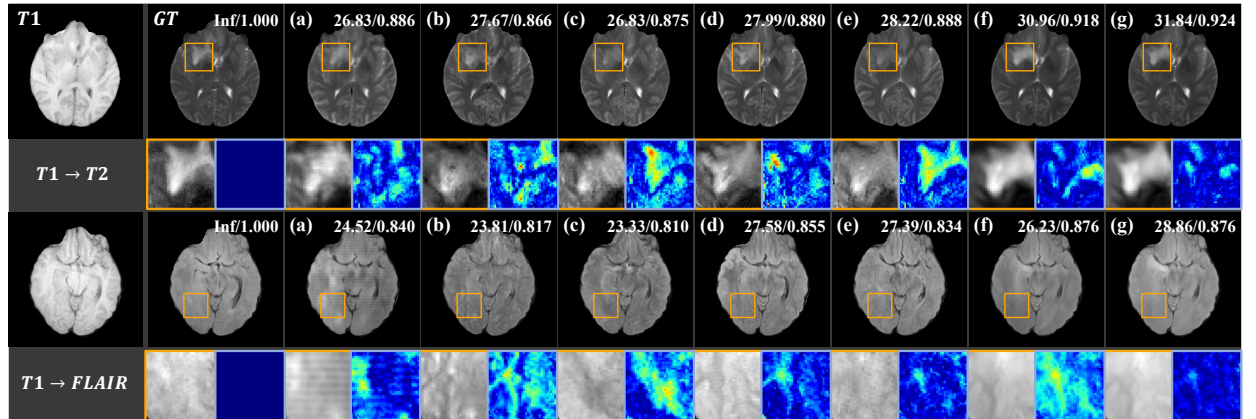


Figure 6: Additional results on BraTs: (a) Ea-GAN, (b) RevGAN, (c) MaskGAN, (d) ResViT, (e) SynDiff (f) DFBK (ours). The first and third rows show the results of T1 to T2 and T1 to FLAIR translation, respectively. The first column is the source image, and the second column is the target ground-truth. The second and fourth rows show the zoomed-in anatomical structures for the first and third rows, respectively. PSNR and SSIM values of each image are shown in the corner of images. The yellow box indicates the zoomed-in visualization area, and the blue box represents the difference heatmap between the generated images and the ground truth. The color indicates the degree of difference from small to large, with the brighter color (e.g., red) reflecting the larger difference and vice versa.

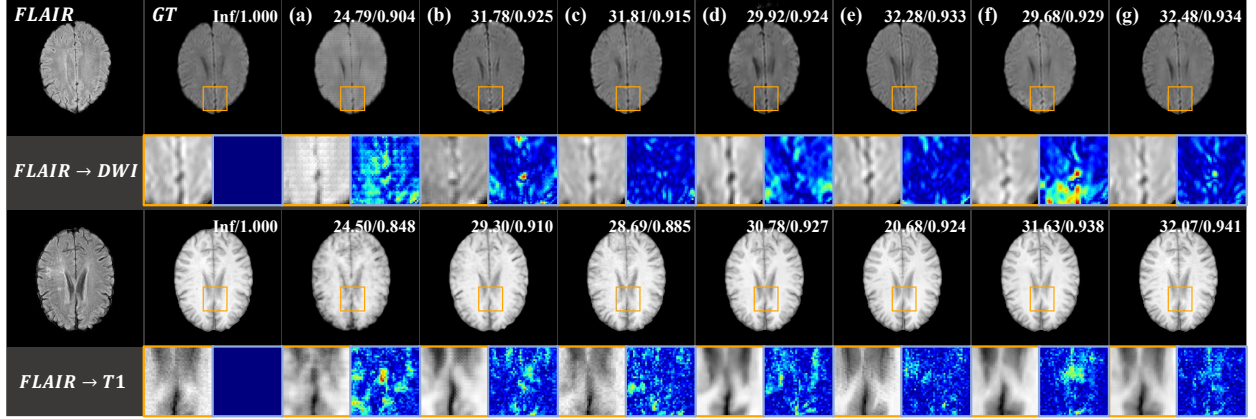


Figure 7: Additional results on ISLES: (a) Ea-GAN, (b) RevGAN, (c) MaskGAN, (d) ResViT, (e) SynDiff (f) DFBK (ours). The first and third rows show the results of FLAIR to DWI and FLAIR to T1 translation, respectively. The first column is the source image, and the second column is the target ground-truth. The second and fourth rows show the zoomed-in anatomical structures for the first and third rows, respectively. PSNR and SSIM values of each image are shown in the corner of images. The yellow box indicates the zoomed-in visualization area, and the blue box represents the difference heatmap between the generated images and the ground truth. The color indicates the degree of difference from small to large, with the brighter color (e.g., red) reflecting the larger difference and vice versa.

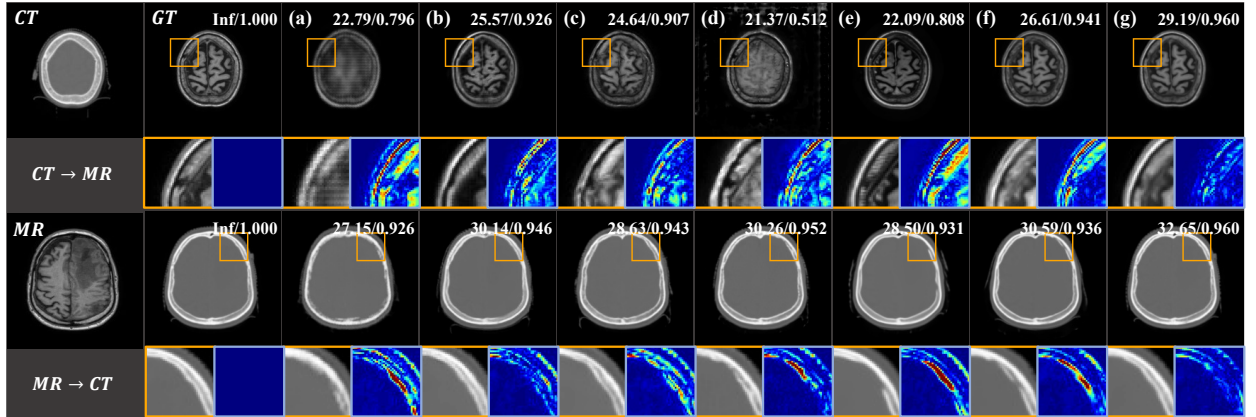


Figure 8: Additional results on SynRAD: (a) Ea-GAN, (b) RevGAN, (c) MaskGAN, (d) ResViT, (e) SynDiff (f) DFBK (ours). The first and third rows show the results of CT to MR and MR to CT translation, respectively. The first column is the source image, and the second column is the target ground-truth. The second and fourth rows show the zoomed-in anatomical structures for the first and third rows, respectively. PSNR and SSIM values of each image are shown in the corner of images. The yellow box indicates the zoomed-in visualization area, and the blue box represents the difference heatmap between the generated images and the ground truth. The color indicates the degree of difference from small to large, with the brighter color (e.g., red) reflecting the larger difference and vice versa.